Glycosylation-driven interactions of nanoparticles with the extracellular matrix: Implications for inflammation and drug delivery

Biomaterials Advances 171 (2025) 214230

Contents lists available at ScienceDirect

Biomaterials Advances

journal homepage: www.journals.elsevier.com/materials-science-and-engineering-c

Glycosylation-driven interactions of nanoparticles with the extracellular matrix: Implications for inflammation and drug delivery☆

Ula von Mentzer, Fritjof Havemeister, Loise Råberg, Hemapriya Kothuru Chinnadurai, Gizem Erensoy, Elin K. Esbjörner, Alexandra Stubelius *

Division of Chemical Biology, Department of Life Sciences, Chalmers University of Technology, Gothenburg, Sweden

ARTICLE INFO

Keywords:
Nanoparticles
Polymeric
Protein corona
Biomolecular corona
Extracellular matrix
Glycosylation
Immunomodulation

ABSTRACT

Cationic nanoparticles (NPs) are emerging as promising carriers for intra-articular drug delivery, particularly for osteoarthritis (OA) where treatment options are limited. However, the clinical translation is challenged by an incomplete understanding of NP interactions within pathological environments. While the influence of the protein coronas on NP behavior has been extensively studied, the specific role of glycoproteins in the extracellular matrix (ECM) remains underexplored, representing a significant knowledge gap. This study investigates how glycosylation-driven interactions between polymeric NPs and enzyme-degraded cartilage biomolecules such as glycosaminoglycans (GAGs) affect NP-ECM aggregate formation and subsequent inflammatory responses. Using an ex vivo model of cartilage degradation induced by catabolic enzymes– hyaluronidase, ADAMTS5 and collagenase– a novel model system was developed to specifically study the behavior of small (<10 nm) and large (~270 nm) cationic NPs in glycoprotein-enriched environments. Atomic force microscopy and dynamic light scattering revealed distinct mesh-like structures formed by the NP aggregates following different enzymatic treatments, confirming the adsorption of glycosylated fragments onto the particles. While total protein content showed minimal differences between NP samples, smaller NPs demonstrated a prominent association with GAGs such as hyaluronic acid and aggrecan, as demonstrated by circular dichroism. These ECM-NP interactions significantly influenced the immunological response, as evidenced by differential cytokine production from macrophages exposed to the aggregates. Our findings underscore the crucial, yet underappreciated, role of glycoproteins in determining NP behavior in pathological environments. Accounting for glycoprotein interactions into the design of nanomaterial and drug delivery systems could significantly improve therapeutic outcomes by enhanced targeting precision, optimized delivery, and effectively modulating immune responses in OA and other complex diseases.

1. Introduction

The increasing prevalence of degenerative joint diseases such as osteoarthritis (OA) presents significant challenges for treatment, with the deterioration of cartilage leading to pain and loss of function [1–3]. Recent advances in OA drug delivery have particularly highlighted the effectiveness of cationic NPs in targeting cartilage [4,5]. Their positive charge facilitates strong electrostatic interactions with negatively charged ECM components, such as glycosaminoglycans (GAG) and proteoglycans. These interactions enhance NP retention, aggregation, and targeted delivery within the dense extracellular matrix (ECM). While neutral and negatively charged NPs may offer distinct interaction profiles and potential safety advantages, their weaker affinity to the ECM limits their effectiveness for cartilage-targeting applications. Instead, small cationic NPs can be designed to penetrate the dense ECM, while large cationic NPs can serve as surface-binding depots [6,7]. However, the success of these delivery systems relies on understanding how NPs interact with the local tissue microenvironment, which can be significantly altered under pathological conditions.

Therapies targeting joint pathologies by local, intra-articular injections first encounter the synovial fluid, a protein-rich ultrafiltrate of plasma that influences their biological fate [8–11]. Rapid adsorption of biomolecules such as proteins, lipids, and metabolites, onto NP surfaces leads to the formation of a biomolecular corona, or more specifically a

☆ This article is part of a special issue entitled: Functional biopolymers published in Biomaterials Advances.

* Corresponding author.
E-mail address: Alexandra.Stubelius@chalmers.se (A. Stubelius).

https://doi.org/10.1016/j.bioadv.2025.214230
Received 23 October 2024; Received in revised form 22 January 2025; Accepted 13 February 2025
Available online 14 February 2025

protein corona (PC), which can significantly affect NP biodistribution, cellular uptake, and immune recognition [12–14]. While the impact of the PC on NP behavior has been well-documented, there is limited understanding of how specific ECM components, particularly glycoproteins, interact with NPs and shape their biological responses [15–17]. Glycosylation, a key post-translational modification, plays a crucial role in immune recognition, cellular uptake, and aggregation. Although most protein corona studies focus on serum proteins, the few investigations into glycosylation coronas have identified specific effects driven by glycostructures, influencing NP-cell interactions and off-target binding [18,19]. Glycoproteins can act as damage-associated molecular patterns (DAMPs) in diseased conditions, with distinct glycosylation patterns critically modulate NP-immune system interactions [20]. This represents an important but understudied factor in the design of nanotherapeutics.

The need to better understand these interactions is especially relevant in OA, where enzymatic degradation of the cartilage ECM leads to the breakdown of GAGs, proteoglycans, and collagen, releasing ECM fragments into the synovial fluid. These degradation products alter the biochemical and biophysical properties of the ECM, compromising tissue integrity and promoting inflammatory signaling [21]. Specifically, fragments such as hyaluronic acid (HA) and chondroitin sulfate increase the anionic charge density within the synovial fluid, which can hinder the diffusion and uptake of cationic NPs by negatively charged cartilage surfaces. Proteoglycan cleavage exposes new binding sites but also disrupts the mesh-like structure of the ECM, affecting NP penetration. Collagen degradation, primarily during advanced stages of OA, further alters the ECM by reducing its structural integrity and creating molecular fragments that interact with NPs in ways distinct from intact collagen fibrils. Our previous study revealed how the different compositions of arthritic patient synovial fluids influenced and hampered the uptake of positively charged NPs into cartilage explants and joint-related cells [22]. Additionally, other studies have shown that the protein adsorption profile varies with health status, and that PC composition correlates with tissue pathology [23,24]. Few studies have specifically investigated the role of glycoproteins in this context, despite their abundance in the ECM and their potential influence on immune responses.

This study aimed to address this gap by investigating how cationic NPs interact not only with proteins, but also with the glycosylation of proteins and other ECM components, as these interactions collectively influence cellular behavior and responses. These large, anionic biomolecules and their formation of a tight mesh have severely hindered development of successful therapies for OA, as they form a dense barrier hindering treatments to reach the deeply embedded chondrocyte, the ECM-producing cell. This study was therefore designed to examine the behavior of cationic polyamidoamine (PAMAM) and poly(lactic-*co*-glycolic acid)-polyethylenimine (PLGA-PEI) NPs in ex vivo porcine articular cartilage explants subjected to enzymatic treatments that simulate the degradative processes of OA. The enzymes hyaluronidase (HYA) and ADAMTS5 (ADA) were included in the model to specifically focus on GAGs, whereas collagenase type II (COL) mainly focused on protein degradation [25–27]. Increased levels of all three enzymes have been found to be active in OA [28–30]. These distinct enzymatic environments allowed us to assess how NP-ECM interactions and subsequent macrophage cytokine responses were influenced by the presence or absence of specific ECM fragments. The use of tissue and cartilage models that closely resemble human cartilage is essential for accurately evaluating NP behaviors such as diffusion and interactions with specific ECM molecules, as they better replicate the dense ECM composition, structure and dimension found in human joints. The results of these studies highlight the importance of incorporating glycoprotein interaction analysis into the development of nanotherapeutic strategies, as the study revealed clear interactions by NPs with GAGs. Understanding these dynamics could significantly improve the design of biomaterials for precision medicine, potentially leading to better therapeutic outcomes for OA and other complex diseases.

2. Results and discussion

2.1. NP and cartilage explant model design and characterization

Size and charge are essential design factors for cartilage targeting, influencing both surface binding and tissue penetration. To investigate these effects, a panel of four NPs with varying sizes and surface charges was developed (Fig. 1). The cartilage ECM is porous and allows the diffusion of small NPs ($\leq$ 15 nm) [9], guiding the synthesis of two dendrimeric PAMAM NPs: $PAMAM_H$ and $PAMAM_L$. $PAMAM_H$ represents an unPEGylated FITC-modified NP, while $PAMAM_L$ was PEGylated to reduce its surface charge. Both are small cationic NPs (<10 nm) with distinct zeta potentials ($PAMAM_H$ = 6.0 nm, +16.5 mV; $PAMAM_L$ = 8.6 nm, +6.4 mV) and were designed to penetrate the full thickness of cartilage tissue. In contrast, larger, polymeric PLGA-based NPs were developed to model drug delivery systems that primarily target the cartilage surface. These larger NPs were synthesized using a nanoprecipitation method, with a hydrophobic PLGA core and amphiphilic $PEG_{20\ 000}$-PEI polymer shell (PEI conjugation confirmed by NMR, Fig. S1, Supporting Information) contributed to their size. By varying the ratios of PEG and PEI, two PLGA-PEI formulations were created: PLGA-PEI_H (270.3 nm, +22.2 mV) and PLGA-PEI_L (265.2 nm, +3.8 mV). The incorporation of PEG reduced charge density, yielding a lower zeta potential in PLGA-PEI_L compared to PLGA-PEI_H. These formulations simulate surface-binding drug delivery strategies, as their larger size prevents penetration into cartilage tissue.

Dynamic Light Scattering (DLS) characterization in solution demonstrated stable, monodisperse NP size distributions for all NP species (Fig. 1A). All NPs also exhibited non-toxicity at the used concentrations (assayed at 500–28 μg/ml) by a resazurin viability assay, as described previously for the PAMAMs [22] and the PLGA-NPs (Fig. S2, Supporting Information). Flow cytometry analysis of uptake efficiency over time revealed that smaller NPs exhibited significantly higher uptake rates compared to the larger particles in both chondrocytes and macrophages (Fig. S3, Supporting Information). The smaller NPs achieved near-complete uptake by chondrocytes within 5 min (~100 %, Fig. S3a), whereas the larger particles required 8 h to exceed 50 % uptake. In macrophages, all particles except PLGA-PEI_L reached 100 % uptake within >8 h, with PLGA-PEI_L achieving only 25 % uptake during the same period (Fig. S3b). These results confirm that both size and charge are important design principles that influence NP cellular uptake kinetics [31].

To assess how specific ECM environments influence NP behavior, we developed a model system designed to simulate complex bioactive ECM conditions associated with OA. The experimental setup ensured a controlled and reproducible environment, mimicking key aspects of OA-associated cartilage degradation [28–30]. While the enzyme concentrations used in this study may not precisely replicate in vivo enzymatic activity—due to the variability in enzyme expression and activity depending on disease severity and patient-specific factors— they were carefully selected to model critical ECM degradation processes. Cartilage explants were preconditioned with proteolytic enzymes to selectively degrade specific ECM components, simulating disease-associated catabolic activity. HYA was used to degrade hyaluronan, ADA to cleave aggrecan (ACAN), and COL to target collagen type II (COL2) [25–27]. This approach enabled the investigation of fundamental mechanisms governing NP-ECM interactions under enzymatically modified conditions, providing insights into how OA-induced ECM changes influence these interactions.

AFM imaging was first used to identify distinct patterns consistent with the expected cartilage degradation products. This confirmed the presence of specific enzyme-generated fragments or the release of nonspecific ECM fragments in the case of the PBS control group (Fig. 1B). In the control group, the majority of released GAGs was

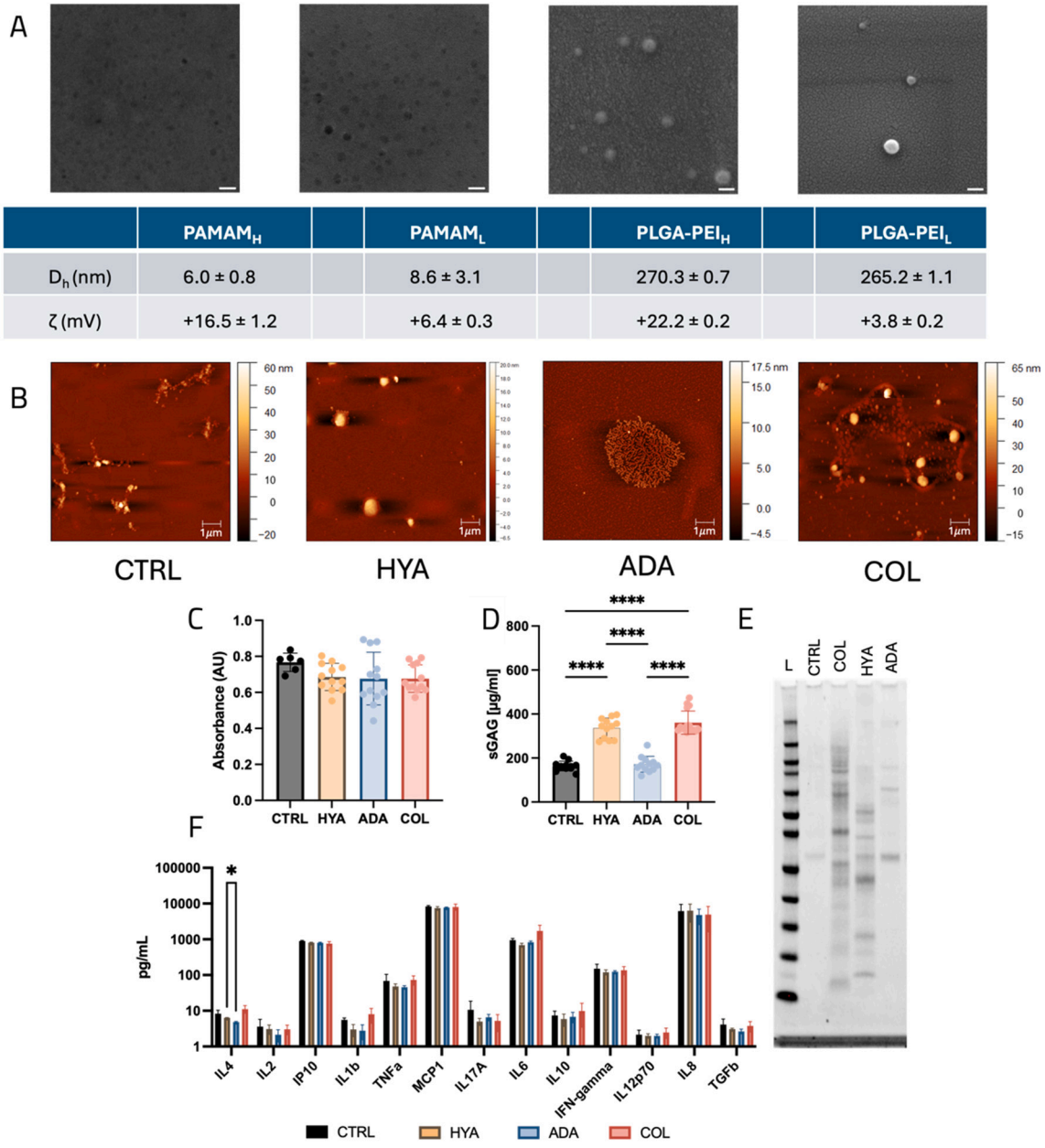

	$PAMAM_H$	$PAMAM_L$	$PLGA\text{-}PEI_H$	$PLGA\text{-}PEI_L$
D_h (nm)	6.0 ± 0.8	8.6 ± 3.1	270.3 ± 0.7	265.2 ± 1.1
ζ (mV)	+16.5 ± 1.2	+6.4 ± 0.3	+22.2 ± 0.2	+3.8 ± 0.2

Fig. 1. Size and charge characteristics of polymeric NP panel and characterization of the ECM-degenerative model. NPs were visualized using TEM for $PAMAM_H$ and $PAMAM_L$ (scale bar = 10 nm) and SEM for $PLGA\text{-}PEI_H$ and $PLGA\text{-}PEI_L$ (scale bar = 100 nm). NP size and zeta potential under aqueous conditions were characterized using DLS and are represented as mean values ± S·D (A). The study includes harvesting cartilage explants from porcine tissue and the characteristics of the supernatants after preconditioning without (PBS control, CTRL) or with catalytic enzymes (Hyaluronidase: HYA, ADAMTS5:ADA, and Collagenase: COL) by AFM (B), total protein content by BCA (C), total sGAG content by the DMMB assay (D), or 1D SDS-PAGE where "L"indicates the protein ladder reference (E). F) Cytokine expression from macrophages stimulated by ex vivo cartilage supernatants from preconditioned explants with CTRL, HYA, ADA, and COL using a multiplex bead assay. Data are represented as mean values ± S.D. Analysis was performed using one-way ANOVA (C and D) or two-way ANOVA (F) with Tukey's multiple comparison post hoc test, where * = $p \leq 0.05$ and **** = $p \leq 0.0001$. N = 6–16 (C and D) or N = 3 biological replicates (F).

attributed to be the products of intrinsic proteases present in the cartilage tissue [30]. HYA-treated cartilage explants mainly released HA which appeared in the supernatants as macroscopic globular condensates with diameters of 0.25–1 µm and heights of 4–21 nm. Cowman and colleagues have previously shown that native HA is composed of long and thin strands with diameters of around 0.5 nm and can appear in several different conformations [32]. In ADA-stimulated explant supernatants, a distinct branched structure of ACAN with a thickness of about 10 nm was observed, in agreement with reports by Ng et al. [33] COL stimulation of the explants mainly resulted in the formation of globular collagen aggregates, however, COL2 fibrils were also observed (Fig. S4, Supporting Information). The round structures may arise as a result of a high degree of collagen degradation caused by multiple cleaving sites of collagen by clostridial collagenase. The mechanism of such degradation has been investigated and reported by Watanabe-Nakayama et al. where similar globular structures were observed when collagen was subjected to type I collagenase cleavage [34].

Total protein content of the supernatants did not change between the conditions including the control (Fig. 1C) To attribute potential differences in protein species between the conditions, 1D SDS-PAGE was used to separate proteins within the 3-260 kDa range, offering a broad spectrum of protein size resolution (Fig. 1E). Smaller protein and

peptide fragments such as cleaved protein fragments can be detected in the lowest range (3–20 kDa), medium sized proteins such as the employed enzymes and structural proteins would be detected in the 20-100 kDa range, and larger proteins such as ECM components and multi-subunit complexes could be detected in the higher ranges. As expected, COL treatment generated the most diverse protein content, while ADA showed the least diversity (Fig. 1E). The quantified sulphated GAG (sGAG) levels in the supernatants of the cartilage explants with or without enzymatic stimulation differed between the treatments (Fig. 1D), whereas the level of induced cytokines did not alter with respect to condition (Fig. 1F).

Taken together, we developed four distinct NPs with unique characteristics to evaluate their interactions with, and behavior across, various biological environments. Our model system utilized enzyme-degraded ECM cartilage to ensure consistent levels of total protein released, while allowing for variations in protein composition and GAGs based on the specific catabolic enzyme used.

2.2. Characterization of NP interactions with released ECM components

While the formation of PCs around NPs in protein-rich environments is well-documented [35], the influence of individual ECM components on NP behavior remains poorly understood. To address this, cartilage explants were preconditioned with the indicated enzymes for 2 h,

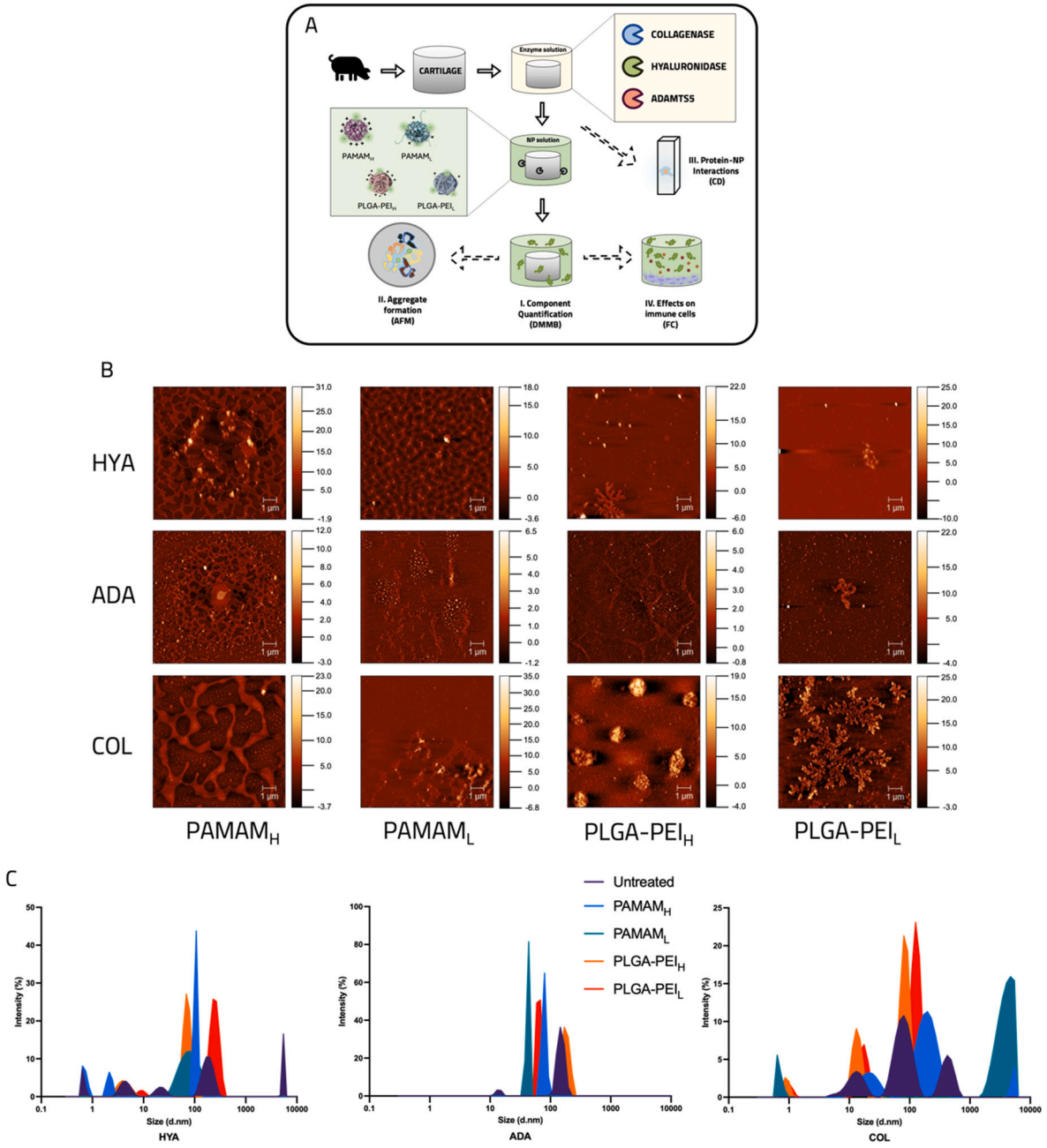

Fig. 2. Study overview and analysis of aggregate formation released ECM components and NPs in enzyme-treated cartilage ex vivo supernatants. The study includes harvested porcine cartilage tissue explants treated with different enzymes and NPs, and the supernatants were analyzed for different ECM-NP interactions by several methods (A). Supernatant samples were deposited on freshly cleaved mica surfaces and dried for AFM analysis (B) or were analyzed in solution by DLS (C) for hyaluronidase (HYA), ADAMTS5 (ADA), and collagenase type II (COL) conditions. AFM Images were acquired using tapping mode AFM. The scale bars on the right of each image represent height in nanometers. The images were analyzed using Gwyddion software (version 2.62) [37].

followed by an additional 2-hour incubation with the NPs to evaluate their interactions within the modified ECM (Schematic overview in Fig. 2A). AFM images revealed mesh-like structures formed upon NP addition, with their morphology varying depending on the specific enzymatic preconditioning (Fig. 2B). DLS analysis further confirmed an increase in NP size after exposure to the supernatants from degraded cartilage, supporting the presence and dimensions of these larger mesh formations (Fig. 2C).

In the HYA treated explants, several protein clusters of varying sizes were detected by DLS. The appearance of mesh-like aggregates was observed by AFM in the explants co-treated with $PAMAM_H$ or $PAMAM_L$, while no such patterns were visible after PLGA NP treatments. $PAMAM_H$-mediated aggregates resulted in sharper peaks compared to the less positive $PAMAM_L$, indicating a stronger charge-dependent biomolecule condensation [36]. This potential charge effect could also be detected by comparing the DLS peaks after co-treatment of the two larger PLGA particles, where PLGA-PEI_H NPs produced smaller, potentially more condensed aggregates compared to PLGA-PEI_L.

Interestingly, ADA treated explants produced a major peak at around 200 nm and a smaller peak at 15 nm by DLS. Although not as prominent as the structures seen in the HYA-treated explants, mesh-like formations were observed by AFM in samples treated with the higher charge NPs $PAMAM_H$ and PLGA-PEI_H. DLS analysis showed that PLGA-PEI_L did not alter the aggregate size, whereas treatment with $PAMAM_L$ produced the smallest aggregates. This suggests that the ADA-generated structure may be influenced by the charge of the NPs, as well as by other factors such as hydrophobic interactions.

The COL preconditioned explants produced three clusters, measured by DLS, at 5–20 nm, 50–100 nm and 300–560 nm. When co-treated with $PAMAM_H$, these aggregates remained as three distinct clusters, shifted towards larger sizes, and were observed by AFM as large meshes alongside small, round aggregates. In contrast, when co-treated with $PAMAM_L$, the majority of the aggregates were found in the 4-5500 nm range by DLS, appearing as less dense and irregular meshes in AFM images. These observations suggest that both small NPs have the capacity to alter the assembly of cleaved collagen, potentially disrupting hydrogen bonding involved in the formation of the collagen alpha helix. COL and PLGA-PEI_H treated samples contained distinct, globular aggregates, visible by AFM but too large to be detected by DLS. Instead, DLS measurements revealed the formation of smaller clusters at 13 nm, and a majority at 100 nm. In contrast, PLGA-PEI_L treatments resulted in highly branched supramolecular structures detected by AFM, whereas by DLS, three clusters appear with a minority at 17 nm and majority at 125 nm, i.e. slightly larger than the ones produced by a more cationic NP. These results suggest that COL-NP aggregate formation may depend on both NP size and surface properties.

The differences in aggregate formation and morphology are primarily driven by the specific ECM components released during enzymatic preconditioning, their interactions with NPs, and the influence of NP charge on the assembly process. DLS measurements showed that HYA and ADA treatments of cartilage resulted in more pronounced size alterations compared to COL, highlighting the significant impact of ECM biomolecules on aggregate formation. Highly charged NPs, such as $PAMAM_H$ and PLGA-PEI_H, formed larger and more condensed aggregates, while less charged NPs, such as $PAMAM_L$ and PLGA-PEI_L, produced smaller, less dense structures. AFM images further confirmed these distinct patterns. These findings emphasize the role of electrostatic interactions in driving aggregate formation, with the ECM composition further modulating aggregate morphology and stability.

2.3. Molecular characterization of the NP-protein aggregates

For a more comprehensive understanding of these NP-ECM interactions, we detailed the protein content of the aggregates. Interestingly, the total quantity of proteins did not change after the addition of different NPs under either ADA or HYA conditions, but changes were observed when co-treated with COL (Fig. 3A-C). This phenomenon did not appear to be charge dependent, as the smaller $PAMAM_H$ did not affect the protein release. Instead, it may be attributed to hydrogen bond interactions between the proline and hydroxyproline residues in collagen fibrils and the PEG surface modification present on all three indicated NPs [27].

SDS-PAGE analysis revealed that NPs did not significantly alter the overall protein composition when compared by molecular weight quantification (Fig. 3D). However, specific changes were observed for individual NPs under certain conditions. For $PAMAM_H$, a new band appeared at 122 kDa in the HYA condition, while a 90 kDa band was absent in the ADA condition. $PAMAM_L$ showed changes in the ADA condition, with new bands at 82 kDa and 66 kDa. For PLGA-PEI_H, a new band emerged at 86 kDa, while a 57 kDa band disappeared in the ADA condition. In the case of PLGA-PEI_L, a single new band was observed at 96 kDa under the HYA condition.

Overall, these changes did not indicate significant differences in the protein composition of the supernatants following NP addition, with no detectable differences observed under the COL condition. While comparing SDS-PAGE results with DLS measurements could provide additional insights on the protein aggregates, the inherent complexity of large molecules such as GAGs makes this comparison challenging [38]. GAGs, due to their molecular shape, can occupy significantly more space relative to their molecular weight, influencing size measurements in nanometers. Additionally, hydrated molecules can exhibit an increased effective size in DLS measurements without any corresponding change in their molecular weight. Moreover, aggregates formed by GAGs and NPs can be detected by DLS due to their hydrodynamic size but may not be distinguishable by SDS-PAGE, which focuses on individual molecular components. Given these limitations, we further analyzed the interactions between specific GAGs and the NPs to gain a deeper understanding of their behavior.

2.4. Glycosaminoglycans and glycoproteins as determinants for NP-ECM interactions

A significant proportion of the PC formed by degraded cartilage ECM could originate from sGAGs. These large structures contribute to cartilage function due to the presence of negatively charged groups that attract water molecules, increasing the ability to absorb and retain water. Although our understanding of NP interactions with fibrous networks such as ECM remains limited, previous research has demonstrated the hindrance of charged particle diffusion within such networks. This hindrance has been attributed to attractive interactions between the oppositely charged structures [39,40]. To investigate the electrostatic interactions between the GAGs and NPs particularly under catabolic conditions, we quantified the sGAG levels in the supernatants of the cartilage explants (Fig. 4 **A-C**). $PAMAM_H$ and $PAMAM_L$ treatment resulted in a decreased sGAG release after degradation by HYA (Fig. 4A) and ADA (Fig. 4B) enzymes. This phenomenon was not observed with the larger, non-penetrating PLGA NPs, suggesting that the ability of small NPs to enter the cartilage ECM could be an important determinant governing NP fate. Additionally, PAMAM dendrimers have been reported to allow intermolecular tethering and utilized as cross-linking agents [41,42]. The possibility of NP-proteoglycan interactions was confirmed in the COL samples, where COL stimulation did not yield a similar pattern in GAG release upon NP addition, and no reduction in sGAGs was detected (Fig. 4C). While COL has been reported to result in the loss of GAGs [43,44], interestingly, we observed a further increase in GAG release after the $PAMAM_H$ addition. Since the mechanism behind such interaction is not currently known, we hypothesize that the synergistic degradation effect may be driven by the disruption in the electrostatic forces that bind GAGs to collagen. Due to their size, highly cationic $PAMAM_H$ may drive a more significant disruption of the matrix structure, making it easier for COL to access collagen and cleave protein-GAG aggregates.

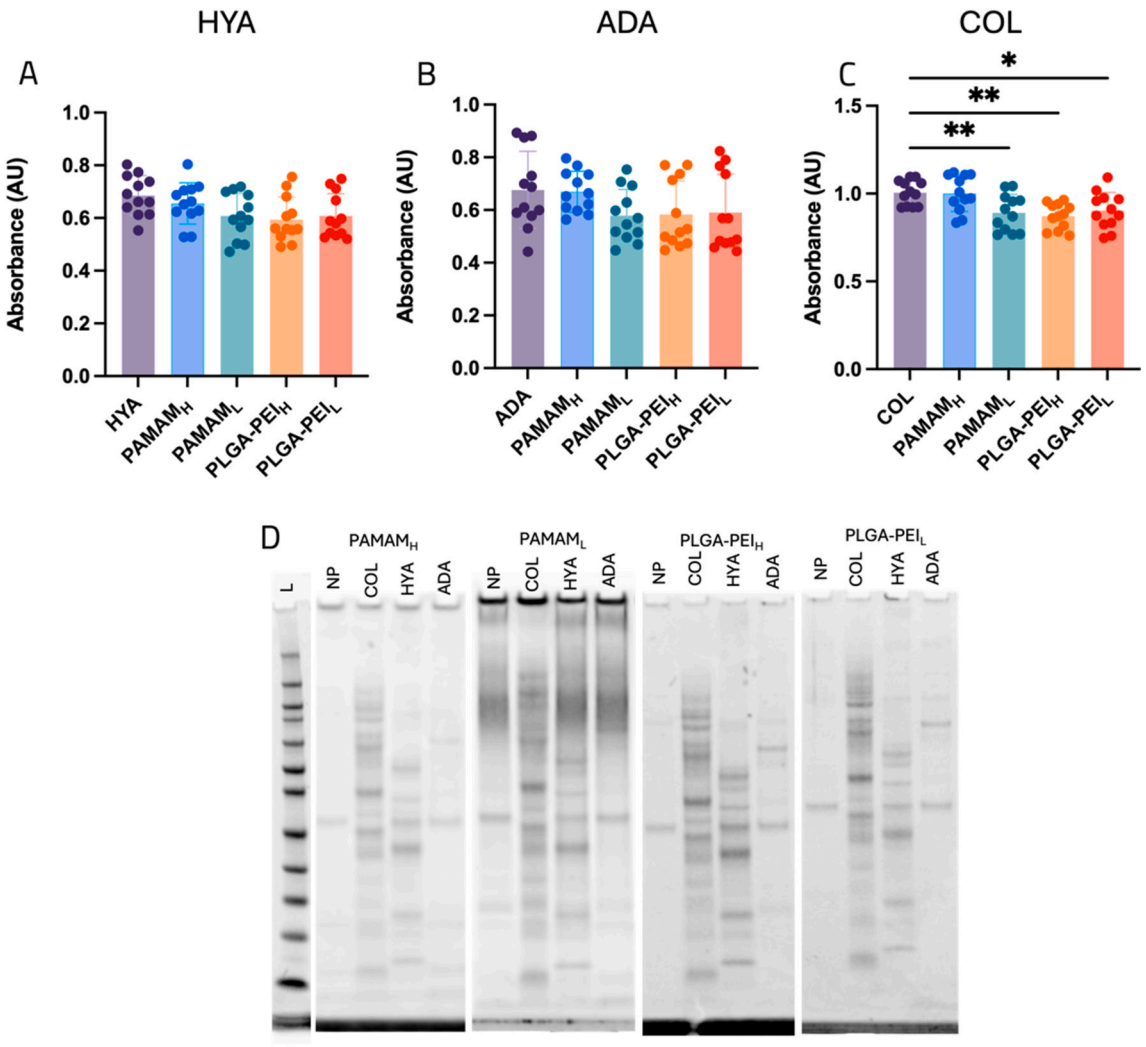

Fig. 3. Protein quantification and protein molecular weight analysis of enzyme-treated cartilage. Overall released protein quantity after hyaluronidase (HYA) (A), ADAMTS5 (ADA) (B), or collagenase type II (COL) (C) enzymatic treatments of explants, quantified by BCA. D) 1D-SDS–PAGE gel of the protein content of the supernatants, where "L" indicates the protein ladder reference, "NP" indicates the specific NP, either under control conditions (CTRL) or with catalytic enzymes as indicated. In A, data are represented as mean values ± S.D. Analysis was performed using one-way ANOVA with Tukey's post hoc test, where * = $p \leq 0.05$, ** = $p \leq 0.01$, $n = 12$.

To determine whether the observed differences in released sGAGs resulted from direct interactions between the NPs and degraded products or an influence of the NPs on enzymatic activity, we employed circular dichroism (CD) spectroscopy to analyze conformational changes in degraded products. CD spectroscopy enabled us to assess the stability and structural characteristics of the sGAGs in the presence of the NPs by detecting alterations in protein secondary structure as well as the chirality of optically active molecules (Fig. 4D-I) [45].

We first measured the CD spectra of the pure biopolymer substrates (HA, ACAN, COL2) as well as their respective enzymes (HYA, ADA, COL) to obtain fingerprints of their secondary structures (Fig. 4D). The CD spectra of the substrates (HA, ACAN, COL2) displayed distinctive CD features, reflecting their chirality. HA showed a strong negative peak around 210 nm, consistent with the CD of GAGs [46]. ACAN displayed fairly weak CD signatures, yet its negative profile below 200 nm suggests the presence of random coil structures. The CD spectrum of COL2 had the distinctive signature of a polyproline helical fold, as expected for collagen. The CD spectra of HYA and ADA suggested that the two enzymes are predominantly α-helical with negative ellipticities at 208 nm and 222 nm, and a positive peak at 193 nm, consistent with published structural data of these two proteins [25,47]. COL displayed a CD spectrum with negative ellipticity at ~210 nm and weak positive ellipticity below 200 nm. This suggested a significant random coil contribution to an otherwise predominant β-sheet structure since COL has a β-sheet rich fold.

Subsequently, the interactions between the NPs with the individual substrates and enzymes were explored by measuring changes to the intrinsic CD spectra (Fig. S5A, Supporting Information). The NPs induced CD spectral shifts for HA (Fig. 4E) and ACAN (Fig. 4F), but not for COL2 (Fig. S5D, Supporting Information). NP-induced spectral shifts were also observed for ADA (Fig. 4G), but not HYA (Fig. S5B, Supporting Information) or COL (Fig. S5C, Supporting Information). To simplify the effect comparisons, we plotted the normalized spectral changes for the substrates (Fig. 4H), and the enzymes (Fig. 4I). This revealed that HA was significantly altered by all NPs likely suggesting a binding interaction, whereas ACAN structural alterations were apparent with PAMAM$_H$ and PAMAM$_L$, but not the larger PLGA-based NPs (Fig. 4H), and ADA was most significantly affected by PAMAM$_H$ and PLGA-PEI$_L$ (Fig. 4I).

Taken together, these results suggest that smaller NPs can interact with several GAGs, particularly in the presence of enzymes that target negatively charged components. This was seen to some extent by DLS, in the DMMB assay which manly measures chondroitin sulfate, as well as the CD spectroscopy, demonstrating direct interactions with HA and ACAN. The ability to interact with these different negatively charged

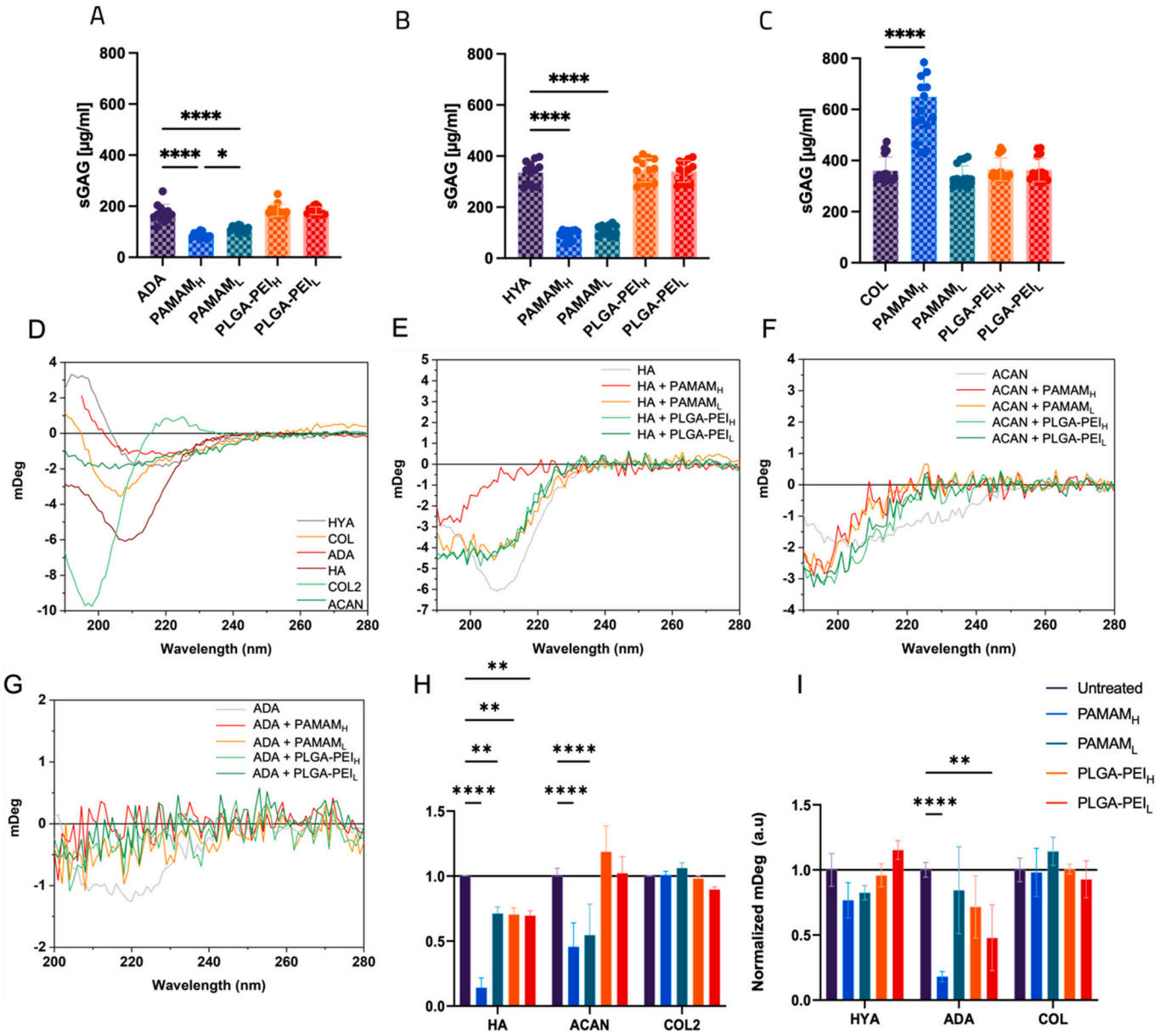

Fig. 4. NP interactions quantified in ex vivo cartilage culture supernatants. The release of sGAGs after the addition of $PAMAM_H$, $PAMAM_L$, $PLGA\text{-}PEI_H$, or $PLGA\text{-}PEI_L$ was measured using a colorimetric change ($\lambda = 525$ nm) for enzymatic explant treatments with hyaluronidase (HYA) (A), ADAMTS5 (ADA) (B), and collagenase type II (COL) (C). Intrinsic CD signatures of the respective biomolecules (D). NPs induced spectral shifts for HA (E), ACAN (F), and ADA (G). The change in CD at the most prominent peak (normalized to the intrinsic CD of each biomolecule) for NP-treated substrates (H) and enzymes (I). The data are represented as mean values ± S.D. Statistical analysis was performed using one-way ANOVA with Tukey's post hoc test, where * = $p \leq 0.05$, ** = $p \leq 0.01$, *** = $p \leq 0.001$, **** = $p \leq 0.0001$.

components of the ECM raises the possibility of the interactions serving as crosslinkers, as previously mentioned, either for soluble proteins or for tissue ECM components. The absence of these interactions with the larger NPs could either be attributed to their overall size, or their larger surfactant corona, which may hinder the NPs' interaction with negatively charged components. The interactions with NPs and products of enzymes that target ampholytic proteins like collagen are more complicated and remain to be studied further, as well as detailed studies on NP interactions with ADA, which seems to neither be size nor charge dependent.

2.5. Macrophage Response to NP-ECM Aggregates

The complex and rich ECM environment composed of several bioactive molecules collectively influence the progression of diseases such as OA. For NPs engineered to deliver therapeutic agents directly to the chondrocyte, the avoidance of being cleared from the joint space and maintain efficient cellular uptake are critical factors that determine the success of drug delivery within the joint. As first responders to the exposure of foreign particles, macrophages play a key role in the regulation of joint homeostasis by clearing tissue debris, mediating cellular communication, and modulating immune responses [48]. Consistent with their critical role, our findings revealed significant differences in NP uptake efficiency. Smaller NPs, such as PAMAMs, demonstrated rapid and higher uptake efficiency in both macrophages and chondrocytes (Fig. S3, Supporting Information). When associated with ECM aggregates such as those formed with COL, the uptake of PAMAMs remained largely unaffected after 8 h (e.g. $PAMAM_H$ from 99.95 % ±0.05 SD to 100 % ±0.0 SD and $PAMAM_L$ from 98.86 % ±1.48 SD to 92.8 % ±12.3 SD, $n = 3$–9). In contrast, the uptake of the larger PLGA-

based particles was significantly reduced in the presence of ECM proteins. This was particularly pronounced for the more cationic PLGA-PEI$_H$ particles, where uptake decreased from 90.9 % ±5.34 SD to 5.98 % ±5.76 SD. The less charged PLGA-PEI$_L$ particles were less affected by ECM proteins but still showed a lower overall uptake (from 25.07 % ±16.58 SD to 10.61 % ±2.99 SD, n = 3–9). These results highlight the critical interplay between size, charge, and ECM association governing NP cellular uptake.

We further investigated whether the catabolic conditions and formed aggregates induced immunomodulatory properties (Fig. 5A-D). Macrophages were stimulated with supernatants from the cartilage explant studies, and the produced cytokines were measured using a multiplex bead assay. The cytokine data is expressed as fold-change relative to no-particle controls to account for background effects of enzymatic preconditioning and ensure that the observed responses primarily reflect NP-ECM interactions.

The highest level of proinflammatory cytokines were observed under the ADA condition, with cytokine production increasing by up to 20-fold compared to the no-particle control (Fig. 5C). Notably, the baseline cytokine levels were similar across all conditions, indicating that the observed cytokine induction was driven by the presence of PAMAM$_H$ or the formation of ECM-NP aggregates. PAMAM$_H$, in particular, triggered elevated levels of IL-1β, a key proinflammatory cytokine activated via the NOD-like receptor family pyrin domain-containing 3 (NLRP3) inflammasome. NLRP3 signaling is known to be activated by particles and crystals, with IL-1β frequently responding to various danger signals [49]. Alternatively, toll-like receptor (TLR) signaling pathways can also induce cytokine responses, as evidenced by increased levels of IL-12 p70 and TGF-β. Elevated levels of these cytokines, which are commonly observed in OA patients, further highlight the proinflammatory potential of PAMAM$_H$ [50–52]. Interestingly, the additional presence of ECM components modulated cytokine profiles. For example, HYA and ADA conditions dampened IL-12 p70 production while enhancing TGF-β levels, suggesting a shift in TLR signaling pathways by these aggregates. In addition, PAMAM$_L$ induced higher TNF-α levels compared to PAMAM$_H$. TNF-α, which synergizes with IL-1β in OA pathophysiology, exhibited condition-dependent variations: ADA conditions increased IL-1β while decreased TNF-α, whereas COL conditions showed the opposite trend. These findings suggest that surface properties, such as PEGylation, and hydrodynamic radius play a significant role in dictating immune responses to PAMAM$_L$.

In contrast, larger PLGA-based NPs induced minimal cytokine production, with PLGA-PEI$_H$ eliciting modest increases in IL-1β and TGF-β. This trend was less evident for PLGA-PEI$_L$, reinforcing the observation that charge, rather than size, is the primary factor influencing immunological responses. This aligns with previous findings that small, highly charged NPs elicit strong immunological responses due to their biomimicry and large surface area-to-volume ratio [53]. Unmodified PAMAM particles, for instance, have been shown to induce cytotoxic responses and cytokine production in a charge-dependent manner, with increasing generation amplifying these effects [54]. Larger particles such as PLGA NPs, designed as controlled release depots, are better suited for minimizing immune interactions This is attributed to their limited ability to penetrate cartilage tissue, their reduced propensity to aggregate with ECM components, and a hydrodynamic radius shielding the NPs from immune cells [53,55]. The surface coating of NPs plays a critical role in determining the NPs interactions with the proteins present in the local microenvironment, as it governs the specific protein species attracted to the particle surface. For example, Chen et al. demonstrated that an appropriate amount of PEI coating enabled plasma proteins to adsorb onto the particle surface without eliciting a significant immune response [56]. Thus, achieving a desirable immune response requires careful tailoring of both the surface coating and the chemical structure of NPs. Our findings further highlight that the ability to attract specific proteins and glycostructures is critical for directing an appropriate and beneficial immune response.

Taken together, our results demonstrated that smaller NPs exhibit significantly higher uptake efficiency compared to larger PLGA-based NPs, both in macrophages and chondrocytes. This higher uptake efficiency, combined with the ability of smaller particles to form stable ECM-NP aggregates, contributes to their more pronounced immunomodulatory effects. Small, highly charged NPs, such as PAMAM$_H$, are suited for therapeutic applications requiring robust ECM penetration and active immunomodulation. However, optimizing surface modifications like PEGylation remains crucial to balance therapeutic efficacy with potential immune activation. Larger NPs, such as PLGA-PEI$_H$ and PLGA-PEI$_L$, offer distinct advantages as drug depots, emphasizing the need for tailored NP designs to address specific therapeutic goals in treating joint disorders.

3. Conclusion

Despite the high potential of NPs to achieve specific targeting and enhanced therapeutic efficacy, their clinical translation often overlooks the complexity of patient-specific disease profiles and the clinical context of conditions like OA. This study investigated how the catabolic environment of OA cartilage affects NP interactions with the ECM, demonstrating that NP behavior is influenced not only by the PC but by the entire extracellular environment, including GAGs, glycoproteins, and soluble factors. These ECM components collectively determine NP aggregation, cellular uptake, and immune responses, making them critical considerations in nanotherapeutic design.

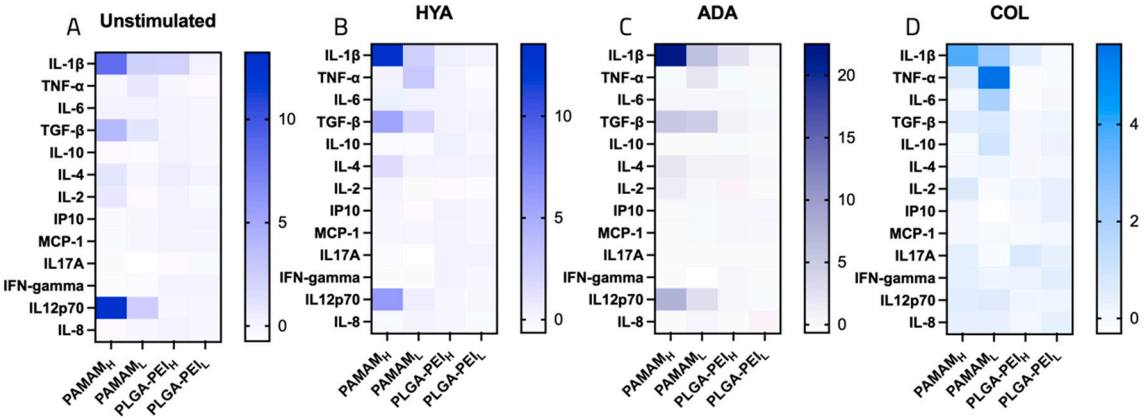

Fig. 5. NP-aggregate effects on macrophage cytokine production. Cytokine production from macrophages was compared after stimulation either with explants treated with media control (A), hyaluronidase (HYA; B), ADAMTS (ADA; C), and collagenase (COL; D) and subsequent treatment of PAMAM$_H$, PAMAM$_L$, PLGA-PEI$_H$ or PLGA-PEI$_L$. Cytokine expression is presented as fold-change relative to no particle controls.

Using an ex vivo catabolic cartilage model, we investigated NP-ECM interactions under enzymatic conditions simulating OA-like environments. While this ex vivo model provided a clinically relevant and controlled platform, it does not fully capture the complexities of in vivo dynamics, including clearance, enzymatic complexities, and contributions of additional cell types to the inflammatory microenvironment. This limitation highlights the need to expand the complexities of future model systems to validate these findings. Nonetheless, the ex vivo system allowed us to identify key mechanisms underlying NP aggregation, diffusion, and immune modulation, offering valuable insights into how glycosylation and material properties influence NP behavior in ECM-rich environments.

Our findings demonstrate that enzymatic degradation of the ECM significantly impacts NP behavior. While NPs exposed to HYA and ADA products exhibited similar effects on GAG release and cytokine induction, COL treatment resulted in markedly different outcomes, highlighting the influence of specific enzymatic conditions. Glycoproteins, abundant in the joint ECM, emerged as critical regulators of NP-ECM interactions by shaping the PC and biomolecular aggregates. Smaller NPs interacted extensively with GAGs, particularly in the presence of enzymes targeting negatively charged ECM components, as evidenced by DLS analysis, DMMB assays, and CD spectroscopy, which confirmed direct interactions with HA and ACAN.

NP aggregation was shown to be driven by interactions with GAG degradation products and glycosylated fragments, which also influenced macrophage cytokine production. Cellular uptake studies revealed a size-dependent retention effect: smaller NPs were minimally affected by ECM aggregation and exhibited enhanced penetration and internalization, while the uptake of larger NPs was significantly hindered. Despite this limitation, larger NPs induced minimal proinflammatory responses, underscoring their suitability for surface-localized drug delivery strategies.

Interestingly, specific glycan structures were found to modulate immune responses, with some reducing proinflammatory effects while others enhanced them. This highlights the importance of designing NPs that account for glycosylation patterns to optimize therapeutic outcomes and control immune activation, and further emphasize the necessity of tailoring drug delivery strategies to align with ECM composition and structural changes during different stages of OA progression.

By elucidating these mechanisms, this study provides a framework for optimizing NP designs to address the unique challenges posed by OA. Small cationic NPs, such as $PAMAM_H$, show promise for applications requiring robust ECM penetration and active immunomodulation, while larger NPs such as PLGA-PEI_H, are better suited as surface-binding drug depots. Future work will build on these findings to explore how material-ECM interactions and glycosylation patterns translate into more complex, clinically relevant models for enhanced therapeutic outcomes. These insights will guide the development of more effective, patient-specific nanotherapeutics, ultimately advancing treatment options for OA and other ECM-rich diseases.

4. Experimental section

4.1. NP synthesis and characterization

PAMAM (G5, ethylenediamine core, Dendritech®, Inc. Sigma Aldrich, Merck KGaA, Darmstadt, Germany) NP synthesis was performed as described previously [23]. Briefly, PEGylation of PAMAMs was performed by combining PAMAM G5 solution (pH = 8) with activated mPEG (1:3; Sigma Aldrich) and allowing it to react for 24 h at room temperature (RT). NPs were fluorescently labeled with fluorescein isothiocyanate (FITC, Sigma Aldrich) (1:5) by allowing the reaction to proceed for 12 h at RT in the dark.

PLGA NPs were synthesized by the nanoprecipitation method. First, the mPEG-PEI polymer was synthesized. To obtain this polymer, PEI (Sigma Aldrich) was dissolved in water and then a 10 % *v*/v solution was prepared with 0.1 M $NaHCO_3$. The pH of the solution was adjusted to approximately 8 with HCl. An equivalent amount of $mPEG_{20000}$-4NPC was solubilized in DMSO (Sigma Aldrich), and mixed with the PEI solution ensuring that DMSO was not >10–20 % of the total solution. The combined mixture was vortexed and covered with foil, incubated for 24 h, and dialyzed (MWCO = 12–14 kDa). Particles were then prepared by the nanoprecipitation method. First, a 1 % solution of polymers ($mPEG_{20000}$-PEI) and PEG_{20000} were dissolved in double distilled water. The ratio between $mPEG_{20000}$-PEI and PEG_{20000} was 1:11 and 1:33 (*w*/w) for PLGA-PEI_H and PLGA-PEI_L NPs respectively. 17 mg/ml PLGA (Sigma Aldrich) solution was prepared in acetone (Fisher Scientific, Waltham USA). 1 ml of the PLGA solution was added onto 50 ml of the polymer solution drop by drop while stirring at 400 rpm at RT for 24 h. FITC labeling was performed as described above using a 10 % ratio compared to the PEI amount in the PLGA solution. The particles were purified using tangential flow, freeze-dried, and stored as a powder in the −20 °C freezer.

All NPs were suspended in dPBS and their hydrodynamic size and zeta potential of NPs were assessed using Zetasizer Nano ZS dynamic light scattering system (Malvern Instruments, UK). The size data was recorded at the 173° scattering angle and 25 °C. $PAMAM_H$ and $PAMAM_L$ sizes are reported based on the number distribution (PDI: 0.02 and 0.13, respectively), while PLGA-PEI_H and PLGA-PEI_L particle size values are reported based on intensity distribution (PDI: 0.20 and 0.11, respectively). NP zeta potential was measured in dPBS. NP size was further analyzed by a scanning electron microscope SEM, JEOL JSM 7800F Prime. NPs were dispersed in double distilled water to 1 mg/ml solution for PLGA-PEI nanoparticles and 30 μM for PAMAM particles that were drop-coated on Mica disc (12 mm, highest grade V1, Ted Pella Inc., Redding, California). The coatings were dried under a vacuum overnight. A 4 nm-thick gold layer sputtered on the dried samples to prevent charging.

NP toxicity was assessed using a resazurin viability assay for 24 h. PAMAM particles were evaluated in human chondrocyte (Tc28a2) and monocyte (U937) cell lines as reported previously [22].

4.2. NP interactions with cartilage tissue

Articular porcine joints were obtained fresh from the Experimental Biomedicine animal facilities under the 3R principle (Gothenburg, Sweden). Prior to explant extraction, cartilage was washed with PBS supplemented with 1 % 10,000 U/ml Penicillin, Streptomycin (Gibco). Cartilage explants were extracted from femoral and tibial condyle cartilage of 3–5-month-old pigs using biopsy punchers (d = 4 mm) while excluding subchondral bone. Explants were placed in 96-well plates, washed three times with supplemented PBS and allowed to equilibrate overnight in DMEM supplemented with 25 mM HEPES under regular cell culture conditions (37 °C, 5 % CO2, 95 % relative humidity).

Explants (n = 12 for each condition) were subjected to enzymatic treatments or PBS control for 2 h including hyaluronidase (250 U/ml), ADAMTS5 (250 nM), and collagenase type 2 (50 U/ml). These concentrations were determined through dose-finding studies to achieve controlled release of GAGs within a specified time frame, ensuring that the tissue was intact. After the enzymatic preincubation, 30 μM NP solution was added to the explants for the next 2 h and the supernatants were harvested and frozen at −20 to −80 °C for further analysis.

4.3. Atomic force microscopy

The supernatants were diluted 1:10 and deposited on freshly cleaved mica, incubated 10 min, rinsed, and air dried overnight. Morphology of the aggregates in the supernatants was investigated using NT-MDT NTEGRA Prima AFM in tapping mode in the air using NSG01 gold-coated single crystal silicon probe (resonant frequency ~150 kHz, force constant ~5.1 N/m). Image analysis was performed in Gwyddion version 2.62.

4.4. Dynamic light scattering of NPs with degraded ECM

The supernatants were diluted to 1:100 in dPBS (Sigma Aldrich) and analyzed as described above.

4.5. Total protein quantification

Protein quantifications were performed on the cartilage explant supernatants. Samples were prepared by a dilution of 1:50, 30s shaking incubation, and then heated for 30 min at 37 °C. The samples were analyzed using the Pierce™ BCA Protein Assay (Thermo Scientific™) according to the manufacturer's instructions. The absorbance was measured at λ562 nm for the BCA assay using a CLARIOstar Plus microplate reader (BMG Labtech, Offenburg, Germany).

4.6. SDS-PAGE

Samples were prepared by combining aliquots from multiple replicate wells ($n = 3$–4). The samples were heated at 37 °C to denature the proteins. A NuPAGE™ 4–12 % Bis-Tris Gel (Invitrogen™ ThermoFisher Scientific, Roskilde, Denmark) was used for the analysis. A total of 7 μl of Novex Sharp Pre-Stained Protein Standard (Invitrogen) was loaded. A 1× MES SDS running buffer was used and the gel was run at 200 V for 35 min. The gel was stained with coomassie staining solution for approximately 30 min and washed and subsequently imaged to visualize the protein bands. The gel was analyzed by Image Lab (BioRad, Hercules, U. S.) for quantitative data on the proteins from the supernatant, comparing the molecular weight of the bands to the ladder.

4.7. Dimehtylmethylene blue (DMMB) assay for sulfated glycosaminoglycan quantification

The 1,9-dimethylmethylene blue (DMMB) assay was performed to quantify the concentration of sGAGs in the samples. A DMMB Solution was prepared by dissolving 8 mg DMMB Zinc Chloride (Sigma Aldrich), 1.52 g glycine (Sigma Aldrich), and 1.185 g NaCl (Sigma Aldrich) in 500 ml MQ water, and pH was adjusted to 3 by 0.1 M HCl. The reagent was vacuum filtered. Samples were diluted 1:4 in the DMMB reagent and a standard curve of chondroitin sulfate in PBS was used to calculate concentrations. Immediately after the DMMB dye had been added to the samples the absorbance was measured at λ525 nm for the DMMB assay using a CLARIOstar Plus microplate reader (BMG Labtech).

4.8. NP cellular uptake by macrophages

Raw 264.7 macrophages cell line (Sigma Aldrich) was used to investigate cellular uptake. The cells were seeded under serum-free conditions at the density of 1×10^5 cells/well, incubated with the NPs for 8 h either with media or supernatants from the COL-treated explants, and washed three times with FACS buffer. Quantification of cellular uptake was performed using a CytoFLEX LX (Beckman Coulter Indianapolis, U.S.) by measuring the FITC signal (λ_{ex} 488 nm/λ_{em} 525/30 nm). Gating included only single, live cells (after FSC/SSC exclusion of dead cells, >5000 cells) with an acquisition range of 5000–10,000 cells. The mean cellular uptake of FITC-labeled NPs was estimated as the average fluorescence intensity of all cells within the gate. All flow cytometry data were analyzed and visualized using FlowJo software V10.

4.9. Monocyte-derived macrophage isolation

Buffy coats were obtained from the blood bank at Sahlgrenska University Hospital (18/23), Gothenburg, Sweden. Approximately 12 ml from six healthy anonymous human donors were collected for PBMC isolation using density gradient centrifugation. Buffy coats were diluted 1:2 in PBS (w/o Ca^{2+}/Mg^{2+}) and then carefully layered over 35 ml Ficoll-paque™ PLUS (Cytiva Sweden AB, Uppsala, Sweden), followed by centrifugation at 400 *g*, for 40 min, at RT. The layer of peripheral blood mononuclear cells (PBMCs) was carefully collected and washed three times using PBS. The purified PBMCs were diluted in RPMI Medium 1640 (Gibco, Paisley, UK) supplemented with 1 % glutaMAX (Gibco, Grand Island, USA), 1 % Penicillin/Streptomycin and 10 % Fetal bovine serum (FBS, Gibco, Paisley, UK). For plastic adhesion, 2×10^8 cells were cultured in a Nunc™ EasYFlask™ 75 cm^2 (ThermoFisher) containing 10 ml supplemented RPMI Medium 1640 with 10 ng/ml macrophage colony-stimulating factor (M-CSF, ThermoFisher Scientific). After 3 h, unattached cells were washed and fresh supplemented RPMI Medium 1640 containing 10 ng/ml M-CSF was added, this procedure was repeated three days later. On day five, the monocyte-derived macrophages (MDMs) were harvested using 2 mL 0.25 % Trypsin-EDTA and a cell scraper. Harvested cells were diluted in fresh supplemented RPMI Medium 1640, pooled, and counted. Differentiated MDMs were plated in 96 well tissue culture plates (VWR®, USA) at a concentration of 5×10^4 cells per well in 150 μl supplemented RPMI Medium 1640. 50 μl supernatants from porcine explants subjected to different enzymes and nanoparticle treatments were added to the MDMs and subsequently incubated for 24 h. Centrifugation at 300 *g* was performed to spin down potential floating cells. MDM supernatants were collected for cytokine quantification and stored at −80 °C.

4.10. Quantification of cytokines

MDM supernatants were examined for quantification of immune response-related targets using the LEGENDplex™ Human Essential Immune Response Panel (Biolegend). The procedure was performed according to the manufacturer's instructions. Briefly, the supernatant was incubated with assay buffer and mixed beads. After incubation for 2 h shaking at 500 rpm, the plate was washed using an assay buffer. Detection antibodies were added to each well and incubated for 1 h shaking. Subsequently, streptavidin-phycoerythrin (SA-PE) solution was added to the wells and incubated an additional 30 min. Finally, the plate was washed twice and immediately read on a flow cytometer. The first run was read on the Guava easyCyte™ and the second run was read on the Beckman Coulter CytoFLEX LX Flow Cytometer. Settings corresponding to the individual flow cytometers used were obtained through the set-up procedure protocols provided by BioLegend. Detection limit of the assay where 9000 pg/ml was the upper limit and 9 pg/ml was the lower limit. Data analysis was performed using the LEGENDplex™ data analysis software. Data is expressed as the fold-change compared to NP untreated controls.

4.11. Interactions between NPs and ECM components

NP-enzyme interactions were studied by monitoring the secondary structure content using CD measurements. All CD measurements were performed on Applied Photophysics Ltd. Chirascan™ using a Hellma Quarts Suprasil® cuvette with 1 mm path length at 25 °C. All spectra were recorded at 190–280 nm, using a 1 nm wavelength increments with a 0.4 s dwell time and a bandwidth of 1 nm. For each sample, 3 individual spectra were recorded, corrected for background contributions by subtracting appropriate blanks, and averaged.

4.12. Statistics

All comparisons between the control and different conditions were performed using either one-way ANOVA of two-way ANOVA with Tukey's post-hoc test using GraphPad Prism 10 (version 10.3.1.).

CRediT authorship contribution statement

Ula von Mentzer: Writing – original draft, Visualization, Project administration, Methodology, Investigation, Formal analysis, Data curation, Conceptualization. **Fritjof Havemeister:** Formal analysis,

Data curation. **Loise Råberg:** Methodology, Investigation, Formal analysis, Data curation. **Hemapriya Kothuru Chinnadurai:** Methodology, Investigation, Data curation. **Gizem Erensoy:** Methodology, Investigation, Formal analysis, Data curation. **Elin K. Esbjörner:** Supervision, Formal analysis, Data curation. **Alexandra Stubelius:** Writing – review & editing, Writing – original draft, Supervision, Project administration, Funding acquisition, Formal analysis, Data curation, Conceptualization.

Declaration of Generative AI and AI-assisted technologies in the writing process

During the preparation of this work the authors used OpenAI for language editing to ensure readability. After using this tool, the authors reviewed and edited the content and take full responsibility for the content of the published article.

Declaration of competing interest

The authors declare that they have no known competing financial interests or personal relationships that could have appeared to influence the work reported in this paper.

Acknowledgements

We would like to express our gratitude to Stefanny de Fatima Guedes Cunha, and Sara Yousefialdashi for their technical assistance. This work was supported by Chalmers Technical University and its Area of Advance Nano. The authors greatly acknowledge further financial support from the Foundation for Sigurd and Elsa Goljes Minne (LA2021-0100), The Royal Swedish Academy of Sciences (CR2021-0024), The Jeanssons Foundation (J2021-0050), The Hasselblad Foundation, the Swedish Research Council (2021-01870), Wilhelm och Martina Lundgrens Vetenskapsfond (2022-4054) the Swedish Rheumatism Association (R-981253), the King Gustaf V's 80-year Foundation (**FAI-2022-0872)** and IngaBritt och Arne Lundbergs Forskningsstiftelse (LU2022-0041).

Appendix A. Supplementary data

Supplementary data to this article can be found online at https://doi.org/10.1016/j.bioadv.2025.214230.

Data availability

Data will be made available on request.

References

[1] Y. Huang, X. Guo, Y. Wu, X. Chen, L. Feng, N. Xie, G. Shen, Nanotechnology's frontier in combatting infectious and inflammatory diseases: prevention and treatment, Signal Transduct. Target. Ther. 9 (1) (2024) 34.
[2] X. Li, X. Peng, M. Zoulikha, G.F. Boafo, K.T. Magar, Y. Ju, W. He, Multifunctional nanoparticle-mediated combining therapy for human diseases, Signal Transduct. Target. Ther. 9 (1) (2024) 1.
[3] T. Zhao, X. Li, H. Li, H. Deng, J. Li, Z. Yang, S. He, S. Jiang, X. Sui, Q. Guo, S. Liu, Advancing drug delivery to articular cartilage: from single to multiple strategies, Acta Pharm. Sin. B 13 (10) (2023) 4127–4148.
[4] A.G. Bajpayee, A.J. Grodzinsky, Cartilage-targeting drug delivery: can electrostatic interactions help? Nat. Rev. Rheumatol. 13 (3) (2017) 183–193.
[5] G.Z. Jin, Current nanoparticle-based Technologies for Osteoarthritis Therapy, Nanomaterials (Basel) 10 (12) (2020).
[6] M. Janssen, G. Mihov, T. Welting, J. Thies, P. Emans, Drugs and polymers for delivery systems in OA joints: clinical needs and opportunities, Polymers 6 (3) (2014) 799–819.
[7] S.P. Schwendeman, R.B. Shah, B.A. Bailey, A.S. Schwendeman, Injectable controlled release depots for large molecules, J. Control. Release 190 (2014) 240–253.
[8] H. Huang, Z. Lou, S. Zheng, J. Wu, Q. Yao, R. Chen, L. Kou, D. Chen, Intra-articular drug delivery systems for osteoarthritis therapy: shifting from sustained release to enhancing penetration into cartilage, Drug Deliv. 29 (1) (2022) 767–791.
[9] X. Li, B. Dai, J. Guo, L. Zheng, Q. Guo, J. Peng, J. Xu, L. Qin, Nanoparticle-cartilage interaction: pathology-based intra-articular drug delivery for osteoarthritis therapy, Nanomicro Lett 13 (1) (2021) 149.
[10] M.F. Rai, C.T. Pham, Intra-articular drug delivery systems for joint diseases, Curr. Opin. Pharmacol. 40 (2018) 67–73.
[11] J. Wen, H. Li, H. Dai, S. Hua, X. Long, H. Li, S. Ivanovski, C. Xu, Intra-Articular Nanoparticles Based Therapies for Osteoarthritis and Rheumatoid Arthritis Management, Mater Today Bio, 2023, p. 100597.
[12] A. Åkesson, M. Cárdenas, G. Elia, M.P. Monopoli, K.A. Dawson, The protein corona of dendrimers: PAMAM binds and activates complement proteins in human plasma in a generation dependent manner, RSC Adv. 2 (30) (2012) 11245–11248.
[13] M.P. Vincent, S. Bobbala, N.B. Karabin, M. Frey, Y. Liu, J.O. Navidzadeh, T. Stack, E.A. Scott, Surface chemistry-mediated modulation of adsorbed albumin folding state specifies nanocarrier clearance by distinct macrophage subsets, Nat. Commun. (2021) 648.
[14] M. Hadjidemetriou, M. Mahmoudi, K. Kostarelos, In vivo biomolecule corona and the transformation of a foe into an ally for nanomedicine, Nat. Rev. Mater. 9 (4) (2024) 219–222.
[15] V. Mirshafiee, R. Kim, M. Mahmoudi, M.L. Kraft, The importance of selecting a proper biological milieu for protein corona analysis in vitro: human plasma versus human serum, Int. J. Biochem. Cell Biol. 75 (2016) 188–195.
[16] J.W. Shreffler, J.E. Pullan, K.M. Dailey, S. Mallik, A.E. Brooks, Overcoming hurdles in nanoparticle clinical translation: the influence of experimental design and surface modification, Int. J. Mol. Sci. 20 (23) (2019) 6056.
[17] R. García-Álvarez, M. Vallet-Regí, Hard and soft protein Corona of nanomaterials: analysis and relevance, Nanomaterials 11 (4) (2021) 888.
[18] A. Ahmad, P.G. Georgiou, A. Pancaro, M. Hasan, I. Nelissen, M.I. Gibson, Polymer-tethered glycosylated gold nanoparticles recruit sialylated glycoproteins into their protein corona, leading to off-target lectin binding, Nanoscale 14 (36) (2022) 13261–13273.
[19] S. Wan, P.M. Kelly, E. Mahon, H. Stöckmann, P.M. Rudd, F. Caruso, K.A. Dawson, Y. Yan, M.P. Monopoli, The "Sweet" Side of the Protein Corona: Effects of Glycosylation on Nanoparticle–Cell Interactions, ACS Nano 9 (2) (2015) 2157–2166.
[20] C. Lambert, J. Zappia, C. Sanchez, A. Florin, J.E. Dubuc, Y. Henrotin, The damage-associated molecular patterns (DAMPs) as potential targets to treat osteoarthritis: perspectives from a review of the literature, Front Med (Lausanne) 7 (2020) 607186.
[21] C. Bonnans, J. Chou, Z. Werb, Remodelling the extracellular matrix in development and disease, Nat. Rev. Mol. Cell Biol. 15 (12) (2014) 786–801.
[22] U. von Mentzer, T. Selldén, L. Råberg, G. Erensoy, A.K. Hultgård Ekwall, A. Stubelius, Synovial fluid profile dictates nanoparticle uptake into cartilage - implications of the protein corona for novel arthritis treatments, Osteoarthr. Cartil. 30 (10) (2022) 1356–1364.
[23] V. Serpooshan, M. Mahmoudi, M. Zhao, K. Wei, S. Sivanesan, K. Motamedchaboki, A.V. Malkovskiy, A.B. Goldstone, J.E. Cohen, P.C. Yang, J. Rajadas, D. Bernstein, Y. J. Woo, P. Ruiz-Lozano, Protein Corona Influences Cell–Biomaterial Interactions in Nanostructured Tissue Engineering Scaffolds, Adv. Funct. Mater. 25 (28) (2015) 4379–4389.
[24] M.J. Hajipour, S. Laurent, A. Aghaie, F. Rezaee, M. Mahmoudi, Personalized protein coronas: a "key" factor at the nanobiointerface, Biomater. Sci. 2 (9) (2014) 1210–1221.
[25] K.L. Chao, L. Muthukumar, O. Herzberg, Structure of human hyaluronidase-1, a hyaluronan hydrolyzing enzyme involved in tumor growth and angiogenesis, Biochemistry 46 (23) (2007) 6911–6920.
[26] N.D.R. Ferreira, C.K. Sanz, A. Raybolt, C.M. Pereira, M.F. DosSantos, Action of hyaluronic acid as a damage-associated molecular pattern molecule and its function on the treatment of temporomandibular disorders, Frontiers in Pain Research 3 (2022).
[27] U. von Mentzer, C. Corciulo, A. Stubelius, Biomaterial integration in the joint: pathological considerations, immunomodulation, and the extracellular matrix, Macromol. Biosci. 22 (7) (2022) e2200037.
[28] B. Grillet, R.V.S. Pereira, J. Van Damme, A. Abu El-Asrar, P. Proost, G. Opdenakker, Matrix metalloproteinases in arthritis: towards precision medicine, Nat. Rev. Rheumatol. 19 (6) (2023) 363–377.
[29] W. Knudson, S. Ishizuka, K. Terabe, E.B. Askew, C.B. Knudson, The pericellular hyaluronan of articular chondrocytes, Matrix Biol. 78-79 (2019) 32–46.
[30] L. Troeberg, H. Nagase, Proteases involved in cartilage matrix degradation in osteoarthritis, Biochim. Biophys. Acta 1824 (1) (2012) 133–145.
[31] M.J. Mitchell, M.M. Billingsley, R.M. Haley, M.E. Wechsler, N.A. Peppas, R. Langer, Engineering precision nanoparticles for drug delivery, Nat. Rev. Drug Discov. 20 (2) (2021) 101–124.
[32] M.K. Cowman, C. Spagnoli, D. Kudasheva, M. Li, A. Dyal, S. Kanai, E.A. Balazs, Extended, relaxed, and condensed conformations of hyaluronan observed by atomic force microscopy, Biophys. J. 88 (1) (2005) 590–602.
[33] L. Ng, A.J. Grodzinsky, P. Patwari, J. Sandy, A. Plaas, C. Ortiz, Individual cartilage aggrecan macromolecules and their constituent glycosaminoglycans visualized via atomic force microscopy, J. Struct. Biol. 143 (3) (2003) 242–257.
[34] T. Watanabe-Nakayama, M. Itami, N. Kodera, T. Ando, H. Konno, High-speed atomic force microscopy reveals strongly polarized movement of clostridial collagenase along collagen fibrils, Sci. Rep. 6 (1) (2016) 28975.
[35] M. Lundqvist, T. Cedervall, Three decades of research about the Corona around nanoparticles: lessons learned and where to go now, Small 16 (46) (2020) e2000892.
[36] T. Bian, A. Gardin, J. Gemen, L. Houben, C. Perego, B. Lee, N. Elad, Z. Chu, G. M. Pavan, R. Klajn, Electrostatic co-assembly of nanoparticles with oppositely

charged small molecules into static and dynamic superstructures, Nat. Chem. 13 (10) (2021) 940–949.
[37] D. Nečas, P. Klapetek, Gwyddion: an open-source software for SPM data analysis, Open Physics 10 (1) (2012) 181–188.
[38] J. Stetefeld, S.A. McKenna, T.R. Patel, Dynamic light scattering: a practical guide and applications in biomedical sciences, Biophys. Rev. 8 (4) (2016) 409–427.
[39] M.J. Grill, J.F. Eichinger, J. Koban, C. Meier, O. Lieleg, W.A. Wall, A novel modelling and simulation approach for the hindered mobility of charged particles in biological hydrogels, Proceedings of the Royal Society A: Mathematical, Physical and Engineering Sciences 477 (2249) (2021) 20210039.
[40] J. Hansing, J.R. Duke 3rd, E.B. Fryman, J.E. DeRouchey, R.R. Netz, Particle diffusion in polymeric hydrogels with mixed attractive and repulsive interactions, Nano Lett. 18 (8) (2018) 5248–5256.
[41] V. Beghetto, V. Gatto, S. Conca, N. Bardella, A. Scrivanti, Polyamidoamide dendrimers and cross-linking agents for stabilized bioenzymatic resistant metal-free bovine collagen, Molecules 24 (19) (2019) 3611.
[42] W.H. Tiong, G. Damodaran, H. Naik, J.L. Kelly, A. Pandit, Enhancing amine terminals in an amine-deprived collagen matrix, Langmuir 24 (20) (2008) 11752–11761.
[43] M. Neidlin, E. Chantzi, G. Macheras, M.G. Gustafsson, L.G. Alexopoulos, An ex vivo tissue model of cartilage degradation suggests that cartilage state can be determined from secreted key protein patterns, PloS One 14 (10) (2019) e0224231.
[44] M.S. Shajib, K. Futrega, T. Jacob Klein, R.W. Crawford, M.R. Doran, Collagenase treatment appears to improve cartilage tissue integration but damage to collagen networks is likely permanent, J Tissue Eng 13 (2022) 20417314221074207.
[45] S.M. Kelly, N.C. Price, The use of circular dichroism in the investigation of protein structure and function, Curr. Protein Pept. Sci. 1 (4) (2000) 349–384.
[46] B. Chakrabarti, E.A. Balazs, Optical properties of hyaluronic acid, Ultraviolet circular dichroism and optical rotatory dispersion, J Mol Biol 78 (1) (1973) 135–141.
[47] L. Mosyak, K. Georgiadis, T. Shane, K. Svenson, T. Hebert, T. McDonagh, S. Mackie, S. Olland, L. Lin, X. Zhong, R. Kriz, E.L. Reifenberg, L.A. Collins-Racie, C. Corcoran, B. Freeman, R. Zollner, T. Marvell, M. Vera, P.E. Sum, E.R. Lavallie, M. Stahl, W. Somers, Crystal structures of the two major aggrecan degrading enzymes, ADAMTS4 and ADAMTS5, Protein Sci. 17 (1) (2008) 16–21.
[48] P. Haubruck, M.M. Pinto, B. Moradi, C.B. Little, R. Gentek, Monocytes, macrophages, and their potential niches in synovial joints – therapeutic targets in post-traumatic osteoarthritis? Front. Immunol. 12 (2021).
[49] Q. Ma, C.S. Lim, Molecular activation of NLRP3 Inflammasome by particles and crystals: a continuing challenge of immunology and toxicology, Annu. Rev. Pharmacol. Toxicol. 64 (Volume 64, 2024) (2024) 417–433.
[50] A.M. Piccinini, K.S. Midwood, DAMPening inflammation by modulating TLR signalling, Mediators Inflamm. 2010 (2010).
[51] L.I. Sakkas, N.A. Johanson, C.R. Scanzello, C.D. Platsoucas, Interleukin-12 is expressed by infiltrating macrophages and synovial lining cells in rheumatoid arthritis and osteoarthritis, Cell. Immunol. 188 (2) (1998) 105–110.
[52] P.M. van der Kraan, Differential role of transforming growth factor-beta in an osteoarthritic or a healthy joint, J Bone Metab 25 (2) (2018) 65–72.
[53] R.E. Hewitt, H.F. Chappell, J.J. Powell, Small and dangerous? Potential toxicity mechanisms of common exposure particles and nanoparticles, Curr Opin Toxicol 19 (2020) 93–98.
[54] I. Durocher, D. Girard, In vivo proinflammatory activity of generations 0-3 (G0-G3) polyamidoamine (PAMAM) nanoparticles, Inflamm. Res. 65 (9) (2016) 745–755.
[55] J.J.M. Lasola, H. Kamdem, M.W. McDaniel, R.M. Pearson, Biomaterial-driven immunomodulation: cell biology-based strategies to mitigate severe inflammation and Sepsis, Front. Immunol. 11 (2020) 1726.
[56] X. Chen, C. Gao, Influences of surface coating of PLGA nanoparticles on immune activation of macrophages, J. Mater. Chem. B 6 (14) (2018) 2065–2077.